Journal of Materials Chemistry C

ROYAL SOCIETY OF CHEMISTRY

PAPER

View Article Online
View Journal

Cite this: DOI: 10.1039/d6tc00101g

350 ps Ultrafast room-temperature scintillation realized on $CsPbBr_3$-based single crystals *via* Br_2 over-doping

Zongxiao Li,[abc] Xiaoping Ouyang,[d] Zhifang Chai,[ac] Duck Young Chung,[e] Fangbao Wang,[d] Yihui He,[h] Tao Bo,[ac] Wenwen Lin *[acef] and Mercouri G. Kanatzidis *[efg]

Ultrafast scintillators are essential for next-generation radiation detection, positron emission tomography, and high-speed medical imaging. All-inorganic $CsPbBr_3$ perovskites are attractive candidates because of their high stopping power, and excellent optical quality, yet their long carrier lifetimes result in slow scintillation responses on the order of hundreds of nanoseconds. Here, we demonstrate that controlled over-doping with Br_2 produces $CsPbBr_{3.03}$ single crystals with sub-nanosecond scintillation at room temperature while preserving crystal quality. Single crystals grown by the Bridgman method exhibit high transparency and maintain the orthorhombic perovskite structure. Br_2 over-doping induces a slight lattice expansion (about 0.42% increase in unit-cell volume) while maintaining the orthorhombic perovskite phase and high optical transparency. Optical absorption reveals a slight redshift of the absorption edge after Br_2 introduction, indicating a modified defect landscape. Time-resolved photoluminescence and radioluminescence measurements show that Br_2 doping creates dense and efficient recombination centers that reduce the scintillation decay time from more than 100 ns in undoped crystals to 350 ps under 5.486 MeV α-particle excitation, and the scintillation decay time decreases by two orders of magnitude. The doped crystals also achieve a spatial resolution of 12 lp mm^{-1} in X-ray imaging. These results reveal a defect-engineering route for achieving ultrafast scintillation in halide perovskites and highlight the potential of Br_2-modified $CsPbBr_3$ for fast timing applications.

Received 13th January 2026,
Accepted 23rd February 2026

DOI: 10.1039/d6tc00101g

rsc.li/materials-c

1. Introduction

A scintillator is a class of materials capable of converting high energy radiation into visible light,[1–3] with extensive applications in nuclear security screening, high energy physics experiments, and medical imaging systems.[4–7] However, the performance of scintillator materials directly determines detector capabilities. An ideal scintillator material should possess the following characteristics:[8,9] (1) high stopping power (elevated effective atomic number, Z_{eff}); (2) short scintillation decay time (*e.g.* few ns); (3) substantial light yield; (4) excellent chemical and thermal stability and facile processability. As shown in Table 1, which summarizes the performance parameters of several conventional scintillator crystals, traditional scintillator materials generally exhibit prolonged luminescence decay times. These over-long >18 ns scintillation decay times limit their applications in ultrafast dynamic medical imaging and ultrafast pulsed radiation detection, which demands ultra-fast scintillation.[10] The scientific community has initiated exploration of novel scintillator materials with sub-nanosecond decay times. Ouyang and co-workers successfully synthesized 2-inch diameter ZnO:Ga crystals *via* hydrothermal methods, achieving an ultrafast scintillation decay time of 600 ps under α particle irradiation.[11] Concurrently, Tao and co-workers realized remarkable performance in $Cs_3Cu_2I_5$:Mn^{2+} single crystals through Mn^{2+} doping, attaining a light yield of

[a] Zhejiang Key Laboratory of Data-Driven High-Safety Energy Materials and Applications, Ningbo Key Laboratory of Special Energy Materials and Chemistry, Laboratory of Advanced Nuclear Materials, Ningbo Institute of Materials Technology and Engineering (NIMTE), Chinese Academy of Sciences, Ningbo 315201, China
[b] University of Chinese Academy of Sciences, Beijing, 100049, China
[c] Qianwan Institute of NIMTE, Ningbo 315336, China
[d] State Key Laboratory of Intense Pulsed Radiation Simulation and Effect and Radiation Detection Research Center, Northwest Institute of Nuclear Technology, Xi'an 710024, China
[e] Materials Science Division, Argonne National Laboratory, Lemont, Illinois 60439, USA
[f] Department of Chemistry, Northwestern University, Evanston, Illinois 60208, USA
[g] Department of Materials Science and Engineering, Northwestern University, Evanston, IL, 60208, USA
[h] State Key Laboratory of Radiation Medicine and Protection, Collaborative Innovation Center of Radiological Medicine of Jiangsu Higher Education Institutions, and School for Radiological and Interdisciplinary Sciences (RAD-X), Soochow University, Suzhou, China

Table 1 Key technical specifications of conventional and commercial scintillator crystals

Materials	Light yield (Photons per MeV)	Decay time (ns)	Scintillation center wavelength (nm)	Energy resolution (%)	Ref.
NaI:Tl	42 000	230	415	5.4 (662 keV)	27,28
CsI:Tl	87 000	800	550	4.8 (662 keV)	27
$Bi_4Ge_3O_{12}$:Ce	8800	300	480	8.52 (662 keV)	29,30
Lu_2SiO_5:Ce	39 000	42	420	9.1 (662 keV)	31
$Gd_3Al_2Ga_3O_{12}$:Ce	28 000	50	515	9.43 (662 keV)	32,33
$(Lu_xY_{1-x})_2SiO_5$:Ce	30 000	42	410	7 (662 keV)	34,35
$LaBr_3$:Ce	63 000	18	358	2.6 (662 keV)	36
(Lu, Gd)AlO_3:Ce	21 000	60	373	14.2 (662 keV)	37
Gd_2SiO_5:Ce, P	11 850	43	450	10.8 (662 keV)	38

95 772 photons/MeV, energy resolution of 3.79% and scintillation decay time of 3 ns under 662 keV γ-ray excitation.[12]

Since 2013, Kanatzidis and co-workers showed that $CsPbX_3$ (X = Cl, Br) perovskite semiconductors function as excellent gamma-ray and X-ray detectors,[13–15] and that their performance stems from properties such as high defect tolerance, long carrier lifetimes, long diffusion lengths, and low-cost crystal growth.[16–20] The octahedral framework of perovskite materials, combined with divalent group-14 cations like Pb^{2+} with their dynamic lone pairs, gives these compounds remarkable defect tolerance and long recombination times. These features make them ideal platforms for further optimization of the material and, ultimately, its radiation detection performance.[21–23] High-quality $CsPbBr_3$ perovskite single crystals were grown using an improved melt-growth method. With an asymmetric electrode design, the resulting semiconductor detectors delivered strong performance, reaching energy resolutions of 1.4% for 662 keV ^{137}Cs and 3.9% for 122 keV ^{57}Co at room temperature.[23,24] Perovskite materials have become a major research focus in both academia and industry, emerging as high-performance, low-cost semiconductor materials for radiation detection.[25] However, their ultrafast scintillation behavior at room temperature remains largely uninvestigated. This work aims to develop perovskite-based scintillators with sub-nanosecond decay times (<1 ns) suitable for room-temperature operation. Previous studies have shown that in high-quality cesium lead bromide single crystals, longer carrier lifetimes result in extended decay times, often reaching hundreds of nanoseconds, highlighting the need for strategies to accelerate recombination dynamics.[26] This study focuses on resolving the key challenge of achieving high crystal quality while simultaneously shortening the scintillation decay time in perovskites. We present a "defect engineering" strategy and grow $CsPbBr_{3.03}$ single crystals with excess Br_2 doping by the vertical Bridgman method. Excess Br_2 introduces efficient exciton recombination centers, which sharply reduces the scintillation decay time without compromising single-crystal quality. This approach yields an ultrafast scintillator with a decay time in the sub-nanosecond regime.

2. Results and discussion

The chemical reagents used in this research include (1) cesium bromide 99.999%, aladdin; (2) lead bromide 99.999%, aladdin; (3) cesium tribromide (synthesized by the chemical reaction of liquid bromine and cesium bromide, as shown in Fig. 1(a). (The details of synthesis are elaborated in the SI, and the PXRD pattern of $CsBr_3$ is presented in Fig. S1).

Stoichiometric amounts of CsBr, $PbBr_2$, and $CsBr_3$ precursors were loaded into quartz tubes for the synthesis of pure-phase $CsPbBr_3$ and $CsPbBr_{3.03}$. During the reaction, the $CsBr_3$ dopant decomposes *in situ* to CsBr and Br_2 gas, introducing bromine into the structure as the active dopant. This approach eliminates the need to handle hazardous elemental bromine directly. The loading of precursors was conducted in a glove box filled with inert gas to prevent impurity contamination. Initially, homogeneous polycrystalline raw materials were synthesized using a tube

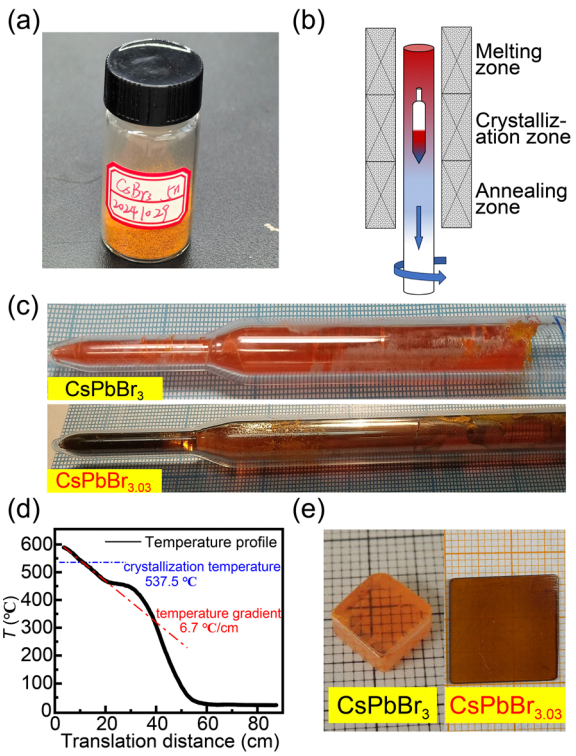

Fig. 1 (a) As-synthesized $CsBr_3$ powder. (b) Schematic diagram of the three-temperature zone vertical Bridgman furnace for single crystal growth. (c) The as-grown single crystal ingots of $CsPbBr_{3.03}$ and $CsPbBr_3$. (d) Temperature-position curve of crystal growth. (e) Polished dark orange $CsPbBr_{3.03}$ and orange $CsPbBr_3$ single crystals.

furnace. Subsequently, the quartz tubes were placed in a vertical gradient freeze furnace for single crystal growth.

Fig. 1(b) schematically illustrates crystal growth by the Bridgman method.[39] Based on the setup shown, the large sealed silica tube is connected to an electric motor that rotates the ingot at 8 rpm while it simultaneously descends at a preset rate. The entire assembly passes sequentially through the melting zone, the crystallization zone, and the annealing zone. Fig. 1(d) presents the temperature profile within the furnace chamber. Based on Fig. 1(b) and (d), the crystal growth process is divided into three steps: first, move downward at a translation rate of 5.0 mm h^{-1} for 14 h before solidification; second, move downward at a translation rate of 0.5 mm h^{-1} for 240 h during solidification; third, move downward at a translation rate of 5.0 mm h^{-1} for 50 h after solidification; finally, downward at a translation rate of 2.0 mm h^{-1} for 60 h for annealing. Under the same synthesis and crystal growth conditions, $CsPbBr_3$ crystals without Br_2 doping were grown as the reference sample. The final obtained crystal ingots are shown in Fig. 1(c). Crystal ingots with excellent light transmittance can be produced by the Bridgman method. After Br_2 doping, the ingots take on a darker, deeper orange hue, in contrast to the bright orange appearance of the undoped crystals. We further performed atomic force microscopy (AFM) on the polished single crystal surfaces (Fig. S2). The white spots correspond to residual polishing agents, while the black lines represent deeper scratches, indicating that abrasives with lower hardness should be used in subsequent polishing. Notably, excessive Br doping did not introduce any special Br rich morphologies, such as pores or well define geometry shapes, on the surface or in the bulk, confirming that doping does not compromise the material's structural integrity.

The two crystals were analyzed by powder X-ray diffraction, which shows only the $CsPbBr_3$ phase. No additional phases are observed upon Br_2 doping. This suggests that the excess bromine does not form a separate crystalline phase and may instead be accommodated within the lattice, for example at interstitial sites. To assess the effect of Br_2 doping on the lattice parameters, the PXRD patterns were refined using TOPAS software.[40] The lattice parameter refinement results are shown in Fig. 2(a) and (b). Table S1 compares the room-temperature lattice constants before and after doping. Br_2 over-doping results in a slight lattice expansion, with increases in *a*, *b*, and *c* and an overall 0.42% increase in unit cell volume. This observation is consistent with the introduction of additional bromine-related species into the lattice, plausibly *via* interstitial incorporation, although complementary chemical and spectroscopic evidence would be needed to identify the specific defect form. Scanning electron microscopy (SEM) characterization was conducted on the $CsPbBr_3$ and $CsPbBr_{3.03}$ samples, as illustrated in Fig. S3. The Br atomic content of the sample $CsPbBr_{3.03}$ is slightly higher than that of the sample $CsPbBr_3$, thus enabling the qualitative confirmation of successful Br_2 doping. Furthermore, elemental mapping results revealed a uniform distribution of Br without observable aggregation or agglomeration.

The DTA curve was measured to examine how excessive Br_2 doping affects both the melting point and the phase transition

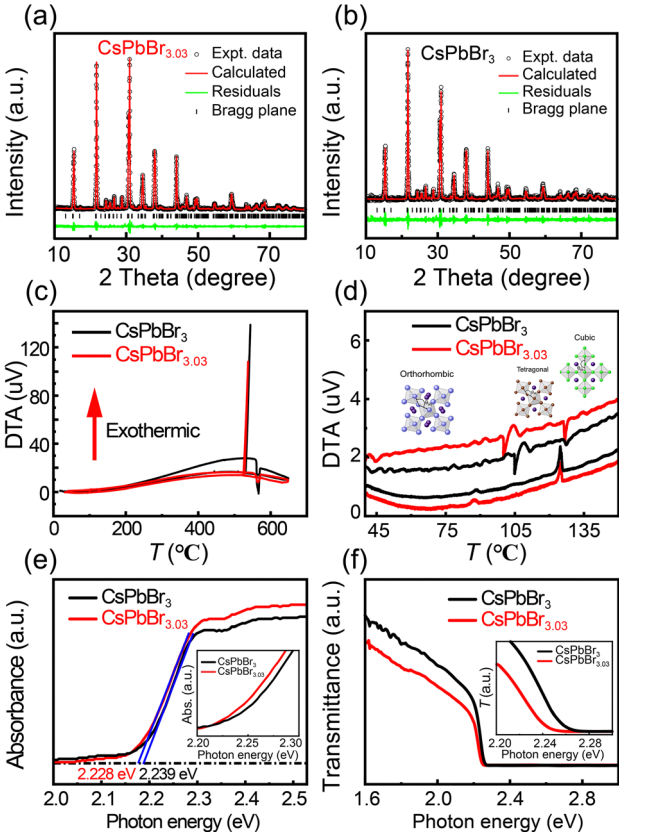

Fig. 2 (a) and (b) TOPAS refinement results of the pure phase $CsPbBr_3$ crystal and Br_2 over-doped $CsPbBr_{3.03}$ crystal. (c) Differential thermal analysis (DTA) curves of $CsPbBr_3$ and $CsPbBr_{3.03}$ crystals from 25 to 650 °C. (d) Differential thermal analysis (DTA) curves of $CsPbBr_3$ and $CsPbBr_{3.03}$ crystals from 40 to 150 °C. (e) UV-Vis optical absorption spectra of $CsPbBr_3$ and $CsPbBr_{3.03}$ crystals. (f) UV-Vis optical transmission spectra of $CsPbBr_3$ and $CsPbBr_{3.03}$ crystals.

temperatures. As shown in Fig. 2(c) and (d), the $CsPbBr_{3.03}$ crystal melts at 564.2 °C and crystallizes at 537.5 °C, while the $CsPbBr_3$ crystal melts at 566.6 °C and crystallizes at 544.0 °C. During the cooling process, $CsPbBr_{3.03}$ crystals undergo phase transitions similar to those of undoped $CsPbBr_3$ crystals. $CsPbBr_{3.03}$ transforms from the cubic phase to the tetragonal phase at 126.9 °C, and then transforms from the tetragonal phase to the orthorhombic phase at 87.2 °C.[41]

Lattice expansion leads to increased atomic spacing, weakening the interatomic interactions, reducing electron wave function overlap, and consequently decreasing the energy required for electrons to transition from the valence band to the conduction band, thereby resulting in a reduced band gap in semiconductor materials.[42–44] Therefore, the band gap of the material was determined by ultraviolet-visible optical absorption spectrum with and without Br_2 doping. Fig. 2(e) shows the comparison diagram of the band gap before and after Br_2 doping. After Br_2 doping, the band gap decreases from 2.239 eV to 2.228 eV. The slight narrowing of the band gap is consistent with the darker color of the $CsPbBr_{3.03}$ crystal. As shown in Fig. 2(f), the reduction of the band gap can also be observed from the transmission spectrum of a finely polished wafer with a thickness of 1.5 mm. Due to

high transparency, both polished crystals have high light transmittance, which is crucial for scintillators to reduce the self-absorption of scintillation light.

To further probe the effect of Br over-doping on the electronic structure of $CsPbBr_3$, X-ray photoelectron spectroscopy (XPS) characterization was performed, as illustrated in Fig. S4. Table S2 summarizes the core-level binding energies of key elements in undoped $CsPbBr_3$ and $CsPbBr_{3.03}$ samples. The most prominent change was observed at the Cs site: the binding energies of the Cs $3d_{5/2}$ and $3d_{3/2}$ peaks decreased systematically by $\sim$3.13 eV, indicative of a notable increase in the electron cloud density around Cs atoms. In contrast, the Pb-Br units forming the perovskite framework remained highly stable: the binding energies of Pb 4f and Br 3d orbitals exhibited negligible shifts ($\leq$ 0.06 eV), all within the instrumental error margin. This distinct selective shift implies that the introduction of excess Br did not significantly perturb the local bonding or electronic structure of the $[PbBr_6]^{4-}$ octahedral framework.

We constructed a $CsPbBr_3$ supercell model and performed calculations using the density functional theory (DFT) method. Specifically, in our modeling Br atoms and Br_2 molecules were introduced at interstitial sites, respectively, with their corresponding three-dimensional configurations depicted in Fig. 3(a)–(c). It is observed that Br and Br_2 reside in the interstitial space among four octahedra, where it exerts mutual compressive interactions with the Cs ions present at this site. Table S3 summarizes the supercells' volumes and formation energies. Notably, when a single interstitial site is occupied by a Br_2 molecule other than Br atom, the volume expansion rate of the model is 0.36%, which is closer to the TOPAS-corrected expansion value of 0.42%. Additionally, the formation energy of the lattice with Br_2 occupancy is 0.164 eV (as the reference state: the formation energy of the undoped model is set to 0), which is significantly lower than the 0.301 eV observed when the site is occupied by Br atoms. Furthermore, the $CsPbBr_3$ cells were removed from the model, leaving only two excess Br atoms. The energies of the two isolated Br atoms and the Br_2 molecule were calculated separately. The results indicate that the energy of Br–Br is −2.847 eV, whereas the energy of the two isolated Br atoms is −0.244 eV. It is evident that the presence of Br in the form of Br_2 within the lattice reduces the formation energy by approximately 1.30 eV per atom, thereby enhancing the structural stability. As observed in Fig. 3(c), excess Br_2 localizes near Cs atomic sites. In comparison to adjacent Pb ions, the occupancy site of Br_2 lies closer to Cs ions. The high electronegativity of Br_2 is likely to induce a reduction in the binding energy of Cs 3d electrons. Consequently, the occupancy environment assumed in the calculations is consistent with the measured results of XPS binding energies.

Excess Br doping can introduce defect levels into the electronic structure, which in turn can significantly alter the background carrier concentration and therefore the resistivity. As shown in Fig. 4(a) and (b), the resistivity of the $CsPbBr_{3.03}$ sample is 1.2×10^{10} Ω cm. After doping, the resistivity decreases significantly to 1.51×10^{8} Ω cm. This two-order-of-magnitude reduction likely reflects an increase in the effective carrier concentration, but it may also arise from changes in defect chemistry and transport associated with Br-rich growth. In particular, the slight lattice expansion could modestly weaken Pb–Br bonding and facilitate ion migration, which can contribute to an apparent increase in conductivity under applied bias. Consistent with this picture, the excess bromine introduced during growth may be accommodated in the lattice, plausibly at interstitial sites, although the specific defect form cannot be established from these measurements alone.

Photoluminescence is a sensitive probe of recombination pathways and defect-related processes in semiconductors. As shown in Fig. 5(a), when excited with a 375 nm laser, the sample emits bright green light. The emission bands of both samples exhibit a full width at half maximum of about 18.0 nm. The PL peak intensity of the $CsPbBr_{3.03}$ sample closely matches that of the $CsPbBr_3$ sample, indicating that Br_2 doping does not quench the luminescence. Our experimental results demonstrate a slight redshift in the optical band gap upon doping, providing evidence that the modified defect environment impacts the electronic structure. However, current measurement techniques are insufficient to resolve the precise nature and energy levels of bromine-induced defects.

To investigate its luminescence dynamics, we first probed the recombination mechanism of the material *via* PL decay measurements. PL decay data were acquired from the emission signals of the two samples at their respective peak wavelengths. Fig. 5(b) and (c) present the time-resolved PL decay curves of

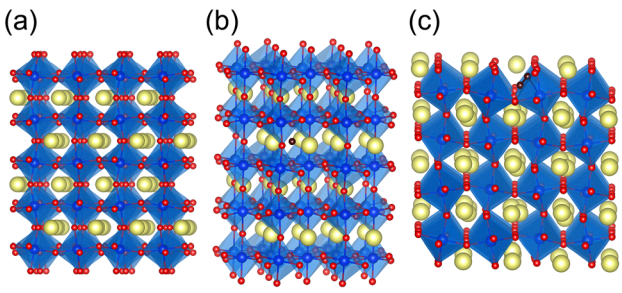

Fig. 3 (a) Schematic illustration of the $2\sqrt{2} \times 2\sqrt{2} \times 2$ supercell structure of $CsPbBr_3$. (b) Schematic illustration of the $2 \times 2 \times 2$ supercell structure of $CsPbBr_3$ doped with one excess Br atom. (c) Schematic illustration of the $2\sqrt{2} \times 2\sqrt{2} \times 2$ supercell structure of $CsPbBr_3$ doped with one excess Br_2.The excess-doped Br atoms are represented by brown symbols.

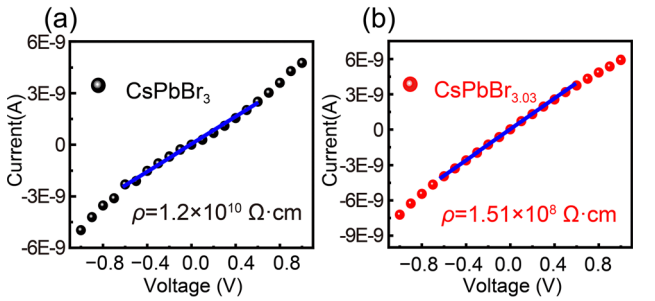

Fig. 4 (a) Current and voltage (I–V) curve of pure phase $CsPbBr_3$ crystals. (b) Current and voltage (I–V) curve of $CsPbBr_{3.03}$ crystals.

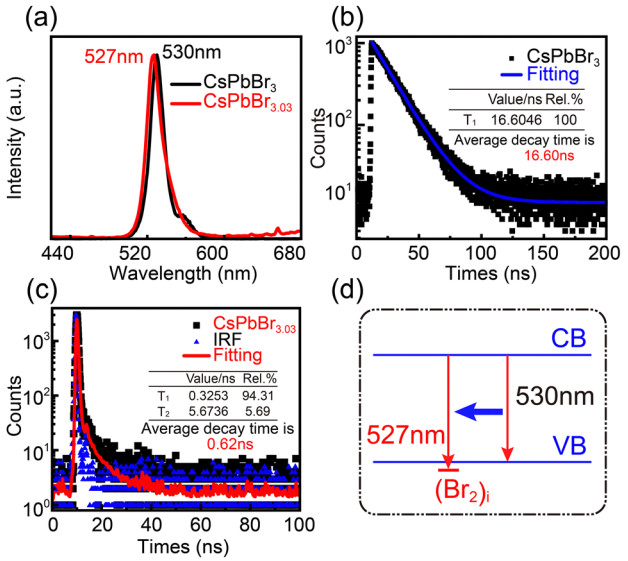

Fig. 5 (a) PL spectra of $CsPbBr_3$ and $CsPbBr_{3.03}$ crystals. (b) Time-resolved PL decay time of the $CsPbBr_3$ crystal under 375 nm laser with a power of 5 mW. (c) Time-resolved PL decay time of the $CsPbBr_{3.03}$ crystal under 375 nm laser with a power of 5 mW. (d) A schematic illustration of the defect charge transition energy levels.

the two samples under 375 nm laser excitation, revealing that the Br_2-doped sample exhibits a notably faster decay rate than the undoped counterpart. The decay curves were fitted using exponential functions, with the relevant fitting parameters summarized in the inset tables of Fig. 5(b) and (c). The Br_2-doped sample shows an average decay time of 0.62 ns, consisting of a fast component (0.31 ns, with a relative amplitude contribution of 94.31%) and a slow component (5.67 ns). The presence of this ultrafast decay component indicates the existence of an extremely rapid radiative recombination pathway within the material. Conventional scintillation processes typically involve multiple sequential steps: ionization radiation generates primary electron–hole pairs; hot carriers relax *via* phonon scattering and other mechanisms; carriers are trapped by luminescent centers; and photons are finally emitted through recombination. Among these steps, carrier relaxation and trap-mediated recombination usually take a relatively long time (ranging from nanoseconds to microseconds). However, the sub-nanosecond ultrafast PL decay observed in this study suggests that under optical excitation, the radiative recombination of the material is dominated by an unconventional ultrafast pathway. This fast pathway may be associated with specific defect states in the material, which allow excitons or carriers to recombine before undergoing complete relaxation and trapping processes. Thus, the ultrafast luminescence component observed in the Br_2-doped sample provides a crucial mechanistic basis for its ultrafast scintillation response. Instead, photoexcitation initially produces a high density of electron–hole pairs in the crystal. The calculations and the fluorescence measurements are consistent with strong electronegativity interstitial Br_2 (Fig. 5(d)) introducing an electron-accepting trap level. In this picture, Br_2 preferentially captures photogenerated electrons (or equivalently withdraws electron density from the host), which suppresses radiative recombination and leaves behind an elevated population of mobile holes in the valence band.

To investigate the potential mechanisms of PL and elucidate the origins of radiative transitions, power-dependent PL spectra were recorded (Fig. 6(a) and (c)). The power-dependent PL spectra of samples $CsPbBr_3$ and $CsPbBr_{3.03}$, measured at room temperature, are displayed in Fig. 6(a) and (c). All spectra exhibit a single emission peak centered at 533 nm and 527 nm, respectively. As shown in Fig. 6(a), the PL intensity increases with rising laser power, indicating a direct correlation between excitation power and emission intensity. This observation offers valuable insights into the underlying radiative recombination mechanisms as follows. As the excitation intensity (L) increases, the PL intensity (I) shows a power-law dependence described by $I \propto L^k$, where the exponent k governs the scaling behavior.[45] When the photon energy of the excitation light exceeds the band-gap energy, the value of the slope k generally falls into one of the following two ranges: $0 < k < 1$ or $1 < k < 2$.[45,46] In the case of $0 < k < 1$, the emission band can be ascribed to donor -acceptor pair recombination (DAP) or free-bound radiative recombination. When $1 < k < 2$, the emission stems from transitions of free excitons or bound excitons.

As shown in Fig. 6(b) and (d), for sample $CsPbBr_3$, the value of k is 1.37, while for sample $CsPbBr_{3.03}$, $k = 1.45$. The k value lies within the scope of free or bound exciton emission. When this is connected with the sub-nanosecond luminescence decay time of sample $CsPbBr_{3.03}$, it can be deduced that the emission mechanism of sample $CsPbBr_{3.03}$ pertains to bound exciton emission.

To conduct a more in-depth study of the exciton–phonon interaction within $CsPbBr_3$ and $CsPbBr_{3.03}$ samples, we

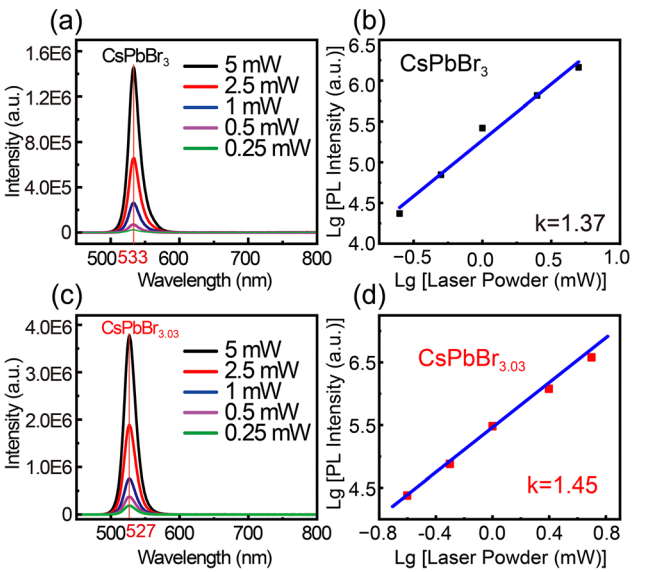

Fig. 6 (a) Power-dependent PL spectra of the $CsPbBr_3$ single crystal at room temperature. (b) Linear fitting of lg (375 nm laser power)-lg (PL intensity) from a cleaved sample of the $CsPbBr_3$ single crystal. (c) Power-dependent PL spectra of the $CsPbBr_{3.03}$ single crystal at room temperature. (d) Linear fitting of lg (375 nm laser power)-lg (PL intensity) from a cleaved sample of the $CsPbBr_{3.03}$ single crystal.

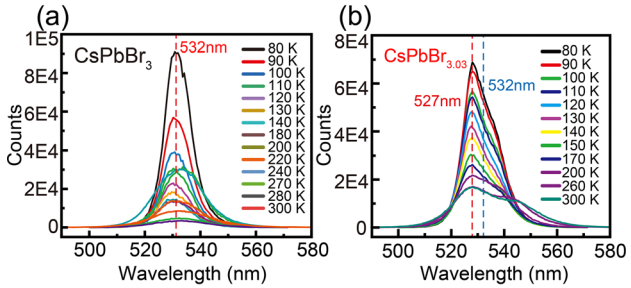

Fig. 7 (a) Temperature-dependent PL spectra of the $CsPbBr_3$ crystal under excitation from a 5 mW 375 nm laser. The emission peak is located near 532 nm. (b) Temperature-dependent PL spectra of the $CsPbBr_{3.03}$ crystal under excitation from a 5 mW 375 nm laser. Each PL spectrum can be deconvoluted into Peak 1 centered at 527 nm and Peak 2 centered at 532 nm.

acquired temperature-dependent PL spectra spanning from 80 K to 300 K (Fig. 7). Owing to phonon-assisted relaxation processes, the intensity of the PL gradually increases as the temperature goes lower. When excited by a 375 nm laser with a power of 5 mW, the PL spectra within this temperature range exhibit a green emission band. As depicted in Fig. 7, the band-edge emission peaks of the $CsPbBr_3$ sample exhibit relatively low sensitivity to temperature. However, the linewidth broadening is attributed to the carrier-LO phonon scattering interaction. For the samples with Br_2 over-doping, a notable redshift of the side peaks at 532 nm is observed.

To gain a deeper understanding of the luminescence mechanism, the relationship between the intensity of the samples' emission peaks and temperature was analyzed using the following formula. The goal was to estimate the thermal activation energy of the sample by fitting the data with the Arrhenius equation:[47]

$$I(T) = \frac{I_0}{1 + Ae^{-E_a/K_B T}}$$

where $I(T)$ and I_0 are the PL intensities at temperatures T and the value at a given temperature. This equation also includes E_a, the thermal activation energy, and K_B, the Boltzmann constant, which has a value of 8.6×10^{-5} eV K^{-1}. Initially, the PL spectra of the samples were subjected to Gaussian peak fitting. The fitting results are presented in Fig. 8. The intensity and FWHM of each peak were meticulously recorded. In addition, the PL peak of sample $CsPbBr_3$ appears symmetric and does not necessitate peak deconvolution, whereas each emission peak of sample $CsPbBr_{3.03}$ can be deconvoluted into two distinct sharp peaks. Subsequently, the aforementioned formula was employed to conduct Arrhenius fitting for these data. The thermal activation energy E_a of the sample $CsPbBr_3$ is estimated to be 33.81 MeV,[48] showing a close proximity to the estimated value of 40 MeV. The thermal activation energy of Sample $CsPbBr_{3.03}$ is estimated at 28.93 MeV and 42.24 MeV, respectively. At 527 nm, the thermal activation energy is lower than that of the undoped sample, indicating the formation of new luminescent centers and the establishment of a more efficient energy transfer pathway. At 532 nm, the thermal activation energy increases, likely because

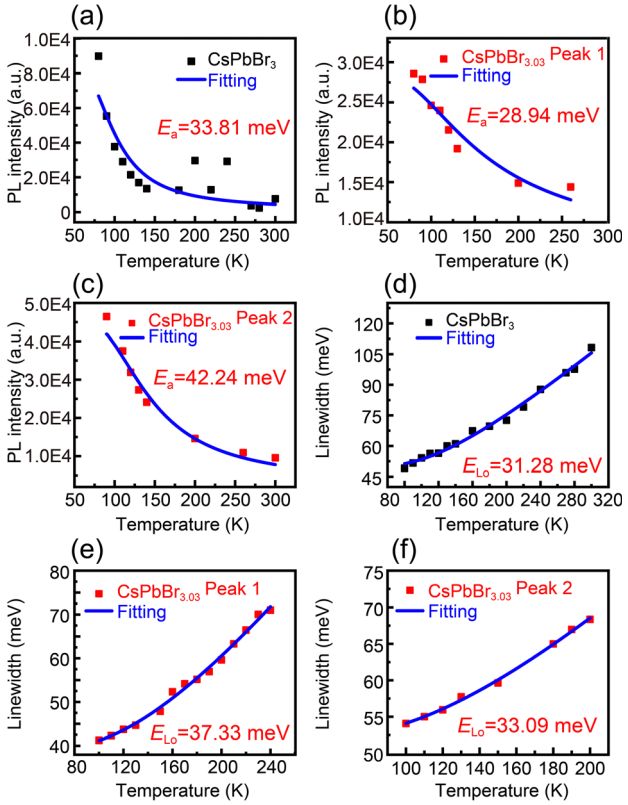

Fig. 8 (a) Arrhenius fitting of the temperature-dependent PL intensity of the $CsPbBr_3$ sample. (b) Arrhenius fitting utilized to analyze the temperature-dependent intensity of peak 1 of sample $CsPbBr_{3.03}$. (c) Arrhenius fitting utilized to analyze the temperature-dependent intensity of the peak 2 of sample $CsPbBr_{3.03}$. (d) Arrhenius fitting used to analyze the temperature-dependent FWHM of the emission peak of $CsPbBr_3$ sample. (e) Arrhenius method used to analyze the temperature-dependent FWHM of the peak 1 in $CsPbBr_{3.03}$. (f) Arrhenius method used to analyze the temperature-dependent FWHM of the peak 1 in $CsPbBr_{3.03}$.

the introduction of Br_2 passivates the original intrinsic luminescent centers, thereby enhancing their stability. On the other hand, the carrier-LO phonon scattering interaction of the samples was explored by measuring the variation of the PL linewidth of the samples with temperature. As depicted in Fig. 7(a) and (b), a notable broadening of the linewidths of both samples was witnessed. This phenomenon can be ascribed to the carrier-LO phonon scattering interaction. For perovskite materials, the temperature-dependent linewidth of PL emission is characterized by the following expression:

$$\Gamma(T) = \Gamma_{\text{inh}} + \Gamma_{\text{LO}}(e^{E_{\text{LO}}/k_B T} - 1)^{-1}$$

Here, the first term, Γ_{inh}, is the inhomogeneous broadening contribution, an Γ_{LO} describes the interactions of carrier-optical phonon contributions to the linewidth broadening. The LO phonon energies (E_{LO}) of the $CsPbBr_3$, $CsPbBr_{3.03}$ peak 1 and $CsPbBr_{3.03}$ peak 2 samples were determined as 31.28, 37.33 and 33.09 MeV, respectively, based on the temperature-dependent PL spectra of the samples. The relatively higher LO phonon energy observed in the Br_2 doped samples implies a more pronounced

scattering interaction between carriers and LO phonons. This phenomenon can be attributed to the fact that Br_2 doping induces lattice expansion. As a consequence, carrier scattering centers are introduced, and the phonon energy is augmented.

To investigate the scintillation behavior of the Br_2-doped samples, we measured the RL spectra and decay curves under excitation by 5.31 MeV α particles from a ^{210}Po source with an activity of 5 mCi. As shown in Fig. 9(a), the emission peaks of the $CsPbBr_{3.03}$ and $CsPbBr_3$ samples are located at 547 nm and 549 nm, respectively. The RL decay time of the samples was tested. As shown in Fig. 9(b) and (c), the average decay time obtained from the time-resolved radioluminescence (TRRL) test of the sample with excessive Br_2 doping at 547 nm is 0.59 ns which is still on the level of sub-nanosecond, and the average decay time of the undoped sample at 549 nm is 122.48 ns.

The performance of the undoped and doped samples in scintillation-based X-ray imaging was evaluated, as depicted in Fig. 10(a) and (b). Upon irradiation with X-rays, both samples presented emission peaks in the vicinity of 540 nm. In comparison with the PL spectra excited by a 375 nm laser, the main emission peak underwent a red shift. As the temperature increases, the energy of the main peak initially rises and then gradually declines. The Br_2 doped sample demonstrated a more intense X-ray radioluminescence than the undoped (approximately 7 times) under a temperature of 7 K and RL conditions, indicating that the radioluminescence intensity was significantly enhanced after bromine doping. This could be attributed to the lower thermal activation energy in the doped system (E_a = 28.94 MeV). Subsequently, X-ray imaging tests were performed on the Br_2 doped samples. Fig. 10(c) shows a schematic diagram of the X-ray imaging system (tube voltage 50 kV). A metal spring enclosed in a black plastic housing was chosen as the imaging subject and positioned between the sample and the X-ray source. Upon X-ray irradiation, the low-density plastic housing was penetrated, whereas the metal effectively blocked the X-rays. The fluorescence image generated by $CsPbBr_{3.03}$ was captured by a CMOS camera equipped with a 20-megapixel sensor. The exposure time was set at 60 s, and the radiation dose rate was 62 mGy s^{-1}, the tube voltage at 50 kV, and the tube current at 1000 μA. X-ray imaging of the item in Fig. 10(d) was carried out using the $CsPbBr_{3.03}$ sample, and the corresponding photographs are presented in Fig. 10(e) and (f). As can be observed, the optimal spatial resolution is around 12 lp mm^{-1}.

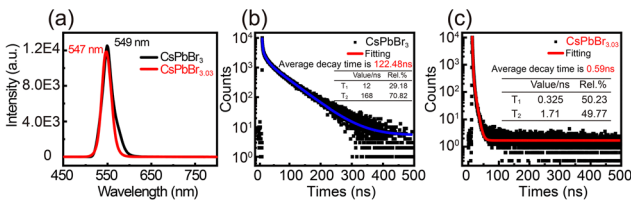

Fig. 9 (a) RL spectra of $CsPbBr_3$ and $CsPbBr_{3.03}$ crystals irradiated by 5.31 MeV α particles (5 mCi). (b) Time-resolved RL decay time of the $CsPbBr_3$ crystal irradiated by 5.31 MeV α particles (5 mCi). (c) Time-resolved RL decay time of the $CsPbBr_{3.03}$ crystal irradiated by 5.31 MeV α particles (5 mCi).

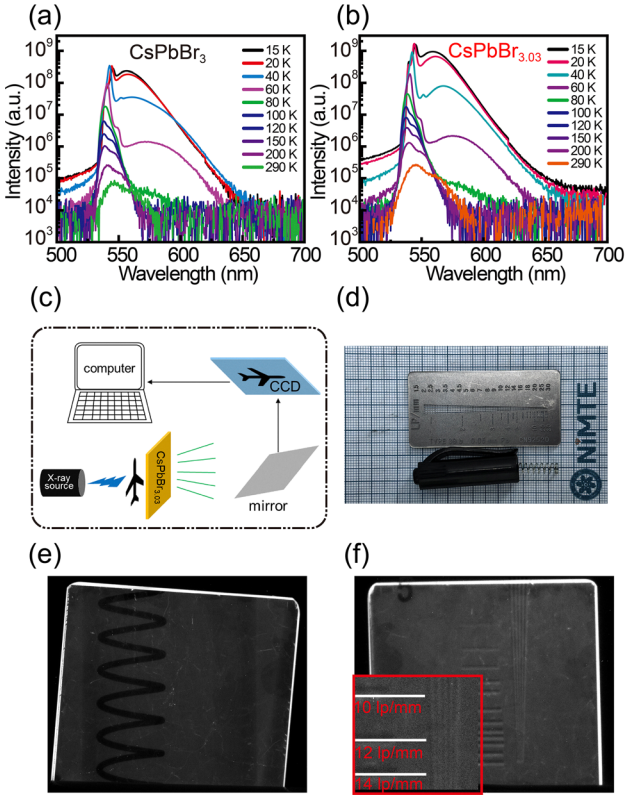

Fig. 10 (a) Temperature-dependent RL spectra of the $CsPbBr_3$ sample excited by X-rays. (b) Temperature-dependent RL spectra of the $CsPbBr_{3.03}$ sample excited by X-rays. (c) Schematic diagram of the X-ray imaging system. (d) The physical image of the spring and wire pair phantom for X-ray imaging. For X-ray imaging applications, the crystal employed has a thickness of 0.8 mm and an area of 16 mm × 17 mm. (e) X-ray fluorescence images of a metallic spring within a black plastic shell. (f) The spatial resolution of the $CsPbBr_{3.03}$ wafer measured by a line pair test pattern.

The aforementioned research findings suggest that $CsPbBr_{3.03}$ single crystals hold promising potential for applications in X-ray imaging.

Due to the gradient variation of Br_2 concentration in the crystal, we observed that the crystals at the tail end exhibited a lower light yield, and $CsPbBr_{3.03}$ was unable to resolve the full energy peak of ^{241}Am α particles (Fig. S5). We attribute this degradation primarily to the increased defect density and non-radiative recombination centers induced by the non-stoichiometric Br_2 excess. This excess Br_2, likely in the form of unreacted precursors or secondary phases (*e.g.*, $CsPb_2Br_5$, Cs_4PbBr_6) at the crystal surface/grain boundaries, could act as effective compound point for charge carriers or excitons. In this scenario, when an excited Br_2 is in close proximity to another Br_2 in the ground state, the excited Br_2 may transfer its energy to the ground state Br_2. As a result, neither of the two Br_2 can emit photons. Instead, the energy is converted into heat and released through lattice vibrations. Moreover, a high doping ratio also enhances the formation of quenching centers within the crystal, which are caused by defects, impurities, *etc.* In addition, the high concentration of luminescent centers shortens the energy

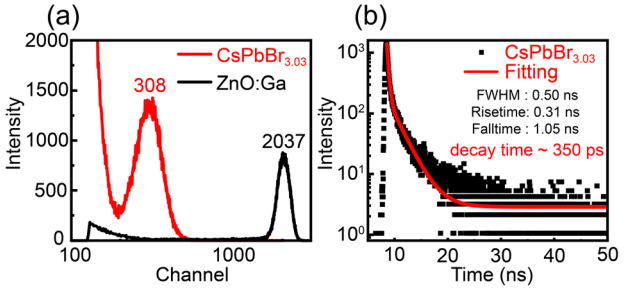

Fig. 11 (a) The pulse height spectra of the $CsPbBr_{3.03}$ samples and the standard sample ZnO:Ga when excited by the 5.486 MeV α particles emitted from ^{241}Am. (The $CsPbBr_{3.03}$ wafer is cut along the growth direction of the crystal ingot). (b) Single-particle time-resolved spectrum of $CsPbBr_{3.03}$ excited by 5.486 MeV α particles emitted from ^{241}Am.

migration path. Consequently, the likelihood that excitations encounter quenching centers increases significantly. We have successfully observed the full energy peak of ^{241}Am α particles in the tip region crystallizing first.

Regarding the measurement of the single particle pulse height spectrum of the $CsPbBr_{3.03}$ samples under α particles excitation, we observed that the channel number of the full energy peak was positively correlated with the scintillation light yield of the specific ray, as shown in Fig. 11(a). When comparing the channel number of the full energy peak of the $CsPbBr_{3.03}$ crystal with that of the commercial scintillator of polycrystalline ZnO:Ga, the former was approximately 15.1% of the latter. Through relative light yield calculations, the light yield of the $CsPbBr_{3.03}$ single crystal was estimated to be ~875 photons/(MeV ns), and the light yield of ZnO employed for comparison is 3333 photons/(MeV ns). The relevant equations are presented as follows:

$$Y_{\text{sample}} = Y_{\text{ref}} \frac{P_{\text{sample}}}{P_{\text{ref}}}$$

where Y represents the light yield and P represents the position of the full energy peak in the energy spectrum. Combined with Fig. S6, the relatively low light extraction efficiency of $CsPbBr_{3.03}$ single crystals can be ascribed to their strong self-absorption effect, as evidenced by the large overlap area between the fluorescence emission and optical absorption spectra of the $CsPbBr_{3.03}$ single crystal sample in Fig. S6. Furthermore, we polished crystals with varying thicknesses and observed that thinning can effectively mitigate the drawback, as illustrated in Fig. S7, From Fig. S7(a)–(c), the resolution improves significantly as the wafer thickness decreases. And an alternative strategy involves enhancing the light yield through doping with rare earth elements as activation ions. Then, we bombarded the $CsPbBr_{3.03}$ wafers with 5.486 MeV α particles sourced from a ^{241}Am radioactive source (11 000 Bq). Fig. 11(b) depicts the typical waveform of the $CsPbBr_{3.03}$ sample acquired using the single photon counting technique. Through effective noise suppression, the superposition of coincidence events was successfully achieved. In Fig. 11(b), the luminescence rise time is 0.31 ns, the FWHM is 0.50 ns, and the decay tail exhibits a two-exponential behavior. This clearly demonstrates that the results accurately reflect the time response characteristics of the sample. By fitting the afterglow curve with the single exponential function:

$$y = y_0 + A_1 e^{-x/t_1} + A_2 e^{-x/t_2} + A_3 e^{-x/t_3}$$

The decay time τ of the $CsPbBr_{3.03}$ single crystal was determined to be approximately 350 ps.

In addition, electrical measurements (see SI, Fig. S8) reveal that heavily Br_2-doped wafers exhibit high dark currents and unstable photo response under applied bias. This behavior is consistent with the presence of a dense population of fast recombination centers and confirms that such doping suppresses long-lived carrier transport. These findings reinforce the interpretation that Br_2 creates molecular-level defects that accelerate recombination for fast timing scintillation but render the material unsuitable for semiconductor detector operation.

3. Conclusions

$CsPbBr_3$-based single crystals with Br-rich conditions (nominal composition $CsPbBr_{3.03}$) were grown from the melt using the vertical Bridgman method, yielding transparent, phase-pure ingots with only a modest lattice expansion relative to undoped $CsPbBr_3$. Br-rich growth introduces a high density of fast recombination pathways that strongly suppress the slow radioluminescence component and enable ultrafast scintillation at room temperature. Under α-particle excitation, the Br-rich crystals exhibit sub-nanosecond radioluminescence dynamics and a single-particle time response with a decay time as short as ~350 ps (compared with the undoped sample, the scintillation decay time reduces by two orders of magnitude), demonstrating that halide perovskites can be driven into a timing regime relevant for fast scintillation and time-resolved detection. In addition, the $CsPbBr_{3.03}$ wafers function as scintillation screens for X-ray imaging, achieving a spatial resolution of ~12 lp mm^{-1} under the conditions tested. At the same time, the electrical measurements indicate that the Br-rich crystals exhibit increased dark current and unstable photoresponse under applied bias, consistent with the introduction of dense recombination centers that accelerate radiative dynamics but degrade long-range charge transport. Therefore, this Br-rich defect-engineering approach is best viewed as a strategy to optimize perovskites for ultrafast scintillation timing rather than for semiconductor detector operation. Future work should focus on identifying the specific bromine-related defect species responsible for the prompt recombination channel, improving compositional uniformity along the ingot, and increasing light yield by mitigating self-absorption and concentration-related quenching while preserving the ultrafast response. At present, we do not understand the microscopic mechanism by which a minute excess of Br drives the scintillation decay into the sub nanosecond regime. Deciphering this will require dedicated future studies, including ultrafast spectroscopy and carrier dynamics modeling, to identify the relevant Br-related defects

and to quantify the carrier generation, transport, trapping, and recombination pathways that set the observed 350 ps response.

4. Author contributions

Z. L. and W. L. designed and accomplished the synthesis, crystal growth, characterization, and measurement of optical properties. Z. L. also conducted data analysis and wrote the manuscript. W. L. designed and supervised the project, and provided assistance in organizing the entire manuscript. Additionally, W. L. carried out the synthesis, crystal growth, doping, and most of the characterization experiments at ANL. Y. H. conducted the γ-ray spectroscopy response tests, Z. C. reviewed, and edited the work. W. L., D. Y. C., and M. G. K. conceived the work and wrote the manuscript. X. O. and F. W. conducted tests on the single photon response of the material. T. B. completed the calculation part.

Conflicts of interest

The authors declare no competing financial interest.

Data availability

The data that support the findings of this study are available from the corresponding author upon reasonable request.

Supplementary information is available. See https://doi.org/10.1039/d5tc00101g.

Acknowledgements

This work was financially supported by the National Natural Science Foundation of China (52272171 and U2267211), the Ningbo Yongjiang Talent Introduction Project (2021A-106-G). At Argonne, the work was supported by the U.S. Department of Energy, National Nuclear Security Administration, Office of Defense Nuclear Nonproliferation Research and Development, and by the U.S. Department of Energy, Office of Basic Energy Sciences, Scientific User Facilities Division, Accelerator and Detector R&D Program under Contract No. DE-SC0020126.

References

1 M. J. Weber, *J. Lumin.*, 2002, **100**, 35–45, DOI: 10.1016/S0022-2313(02)00423-4.
2 G. Blasse and B. C. Grabmaier, *Lumin. Mater.*, 1994, 1–9, DOI: 10.1007/978-3-642-79017-1.
3 T. Yanagida, *Proc. Jpn. Acad. Ser. B Phys. Biol. Sci.*, 2018, **94**, 75–97, DOI: 10.2183/pjab.94.007.
4 P. Lecoq, *NIM-A: Accelerators, Spectrometers, Detectors and Associated Equipment*, 2016, **809**, 130–139, DOI: 10.1016/j.nima.2015.08.041.
5 L. Yi, B. Hou, H. Zhao and X. Liu, *Nature*, 2023, **618**, 281–286, DOI: 10.1038/s41586-023-05978-w.
6 K. Sakhatskyi, B. Turedi, G. J. Matt, E. Wu, A. Sakhatska, V. Bartosh, M. N. Lintangpradipto, R. Naphade, I. Shorubalko, O. F. Mohammed, S. Yakunin, O. M. Bakr and M. V. Kovalenko, *Nat. Photonics*, 2023, **17**, 510–517, DOI: 10.1038/s41566-023-01207-y.
7 J.-L. Wang, X.-G. Wu, Z.-Y. He, L.-W. Yang, Y. Zheng, C.-B. Li, T.-X. Li and Z.-H. Zhao, *Eng. Res. Express*, 2024, **6**, 025328, DOI: 10.1088/2631-8695/ad43b4.
8 T. Martin, A. Koch and M. Nikl, *MRS Bull.*, 2017, **42**, 451–457, DOI: 10.1557/mrs.2017.116.
9 F. Zhou, Z. Li, W. Lan, Q. Wang, L. Ding and Z. Jin, *Small Methods*, 2020, **4**, 2000506, DOI: 10.1002/smtd.202000506.
10 C. Ronda, *Opt. Mater.: X*, 2024, **22**, 100293, DOI: 10.1016/j.omx.2024.100293.
11 R. Lin, Y. Zhu, L. Chen, W. Zheng, M. Xu, J. Ruan, R. Li, T. Li, Z. Lin, L. Cheng, Y. Ding, F. Huang and X. Ouyang, *PhotoniX*, 2022, **3**, 9, DOI: 10.1186/s43074-022-00054-4.
12 Q. Yao, J. Li, X. Li, Y. Ma, H. Song, Z. Li, Z. Wang and X. Tao, *Adv. Mater.*, 2023, **35**, 2304938, DOI: 10.1002/adma.202304938.
13 L. Pan, K. S. Bayikadi, I. R. Pandey, S. Karki, Z. Liu, J. A. Peters, M. De Siena, D. Y. Chung, B. W. Wessels and M. G. Kanatzidis, *Adv. Mater. Technol.*, 2025, **10**, 2401548, DOI: 10.1002/admt.202401548.
14 K. S. Bayikadi, Z. Liu, J. A. Peters, I. Pandey, P. Q. Vuong, S. Imam and M. G. Kanatzidis, *Adv. Mater.*, 2025, **37**, e10931, DOI: 10.1002/adma.202510931.
15 L. Pan, I. R. Pandey, A. Miceli, V. V. Klepov, D. Y. Chung and M. G. Kanatzidis, *Adv. Opt. Mater.*, 2023, **11**, 2202946, DOI: 10.1002/adom.202202946.
16 Y. He, L. Matei, H. J. Jung, K. M. McCall, M. Chen, C. C. Stoumpos, Z. Liu, J. A. Peters, D. Y. Chung, B. W. Wessels, M. R. Wasielewski, V. P. Dravid, A. Burger and M. G. Kanatzidis, *Nat. Commun.*, 2018, **9**, 1609, DOI: 10.1038/s41467-018-04073-3.
17 G. Li, H. Wang, Z. Zhu, Y. Chang, T. Zhang, Z. Song and Y. Jiang, *Chem. Commun.*, 2016, **52**, 11296–11299, DOI: 10.1039/c6cc05877a.
18 C. C. Stoumpos, C. D. Malliakas, J. A. Peters, Z. Liu, M. Sebastian, J. Im, T. C. Chasapis, A. C. Wibowo, D. Y. Chung, A. J. Freeman, B. W. Wessels and M. G. Kanatzidis, *Cryst. Growth Des.*, 2013, **13**, 2722–2727, DOI: 10.1021/cg400645t.
19 L. Pan, Z. Liu, C. Welton, V. V. Klepov, J. A. Peters, M. C. De Siena, A. Benadia, I. Pandey, A. Miceli, D. Y. Chung, G. N. M. Reddy, B. W. Wessels and M. G. Kanatzidis, *Adv. Mater.*, 2023, **35**, 2211840, DOI: 10.1002/adma.202211840.
20 L. Pan, Y. He, V. V. Klepov, M. C. De Siena and M. G. Kanatzidis, *IEEE TMI*, 2022, **41**, 3053, DOI: 10.1109/TMI.2022.3176801.
21 Y. Zhou, C. Fei, M. A. Uddin, L. Zhao, Z. Ni and J. Huang, *Nature*, 2023, **616**, 712–718, DOI: 10.1038/s41586-023-05847-6.
22 B. R. C. Vale, D. Scolfaro, C. A. Sousa, A. F. V. Fonseca, L. G. Bonato, A. F. Nogueira, J. Bettini and L. A. Padilha, *ACS Appl. Nano Mater.*, 2025, **8**, 4373–4383, DOI: 10.1021/acsanm.4c04839.
23 Y. He, M. Petryk, Z. Liu, D. G. Chica, I. Hadar, C. Leak, W. Ke, I. Spanopoulos, W. Lin, D. Y. Chung, B. W. Wessels,

Z. He and M. G. Kanatzidis, *Nat. Photonics*, 2021, **15**, 36–42, DOI: 10.1038/s41566-020-00727-1.
24 Y. He, L. Matei, H. J. Jung, K. M. McCall, M. Chen, C. C. Stoumpos, Z. Liu, J. A. Peters, D. Y. Chung, B. W. Wessels, M. R. Wasielewski, V. P. Dravid, A. Burger and M. G. Kanatzidis, *Nat. Commun.*, 2018, **9**, 1609, DOI: 10.1038/s41467-018-04073-3.
25 Y. He, I. Hadar and M. G. Kanatzidis, *Nat. Photonics*, 2022, **16**, 14–26, DOI: 10.1038/s41566-021-00909-5.
26 D. Y. Chung, W. Lin, M. Unal, Q. V. Phan, I. R. Pandey, R. Vitt, Y. He and M. G. Kanatzidis, *Cryst. Growth Des.*, 2024, **24**, 9590–9600, DOI: 10.1021/acs.cgd.4c01109.
27 R. Hawrami, E. Ariesanti, A. Farsoni, D. Szydel and H. Sabet, *Crystals*, 2022, **12**, 1517, DOI: 10.3390/cryst12111517.
28 N. T. Luan, K. H. Joo, L. H. Su, J. Jegal, L. T. Truc, K. Arshad and N. D. Ton, arXiv, 2024, *preprint*, arXiv:2404.18551, DOI: 10.48550/arXiv.2404.18551.
29 A. Phunpueok, V. Thongpool, S. Jaiyen and H. S. Hsu, *Appl. Mech. Mater.*, 2020, **901**, 89–94, DOI: 10.4028/www.scientific.net/amm.901.89.
30 Y. Tang, M. Deng, Q. Liu, C. Kang, X. Li, J. Zheng, K. Suenaga, Z. Zhou, J. Chen, J. Wang and Q. Liu, *Adv. Opt. Mater.*, 2023, **12**, 2301332, DOI: 10.1002/adom.202301332.
31 Y. Wu, M. Tian, J. Peng, M. Koschan, I. Greeley, C. Foster and C. L. Melcher, *Phys. Status Solidi RRL*, 2018, **13**, 1800472, DOI: 10.1002/pssr.201800472.
32 Y. Zhu, S. Qian, Z. Wang, H. Guo, L. Ma, Z. Wang and Q. Wu, *Opt. Mater.*, 2020, **105**, 109964, DOI: 10.1016/j.optmat.2020.109964.
33 G. Della Casa, N. Zampa, D. Cirrincione, S. Monzani, M. Baruzzo, R. Campana, D. Cauz, M. Citossi, R. Crupi, G. Dilillo, G. Pauletta, F. Fiore and A. Vacchi, *Nucl. Instrum. Methods Phys. Res. A*, 2024, **1058**, 168825, DOI: 10.1016/j.nima.2023.168825.
34 P. Mengucci, G. Andre, E. Auffray, G. Barucca, C. Cecchi, R. Chipaux, A. Cousson, F. Davi, N. D. Vara, D. Rinaldi and E. Santecchia, *Nucl. Instrum. Methods Phys. Res. A*, 2015, **785**, 110–116, DOI: 10.1016/j.nima.2015.02.061.
35 V. Kalinnikov, E. Velicheva and Y. Uozumi, *Phys. Part. Nuclei Lett.*, 2021, **18**, 457–468, DOI: 10.1134/S1547477121040105.
36 Y.-Y. Ji, T. Lim and W. Lee, *J. Radiat. Prot. Res.*, 2018, **43**, 85–96, DOI: 10.14407/jrpr.2018.43.3.85.
37 M. Pokorný, V. Babin, A. Beitlerová, K. Jurek, J. Polák, J. Houžvička, D. Pánek, T. Parkman, V. Vaněček and M. Nikl, *NPG Asia Mater.*, 2021, **13**, 66, DOI: 10.1038/s41427-021-00332-w.
38 M. V. Belov, Y. D. Zavartsev, M. V. Zavertyaev, A. I. Zagumennyi, V. A. Kozlov, S. A. Kutovoi, N. V. Pestovskii and S. Y. Savinov, *B. Lebedev Phys. Inst.*, 2020, **47**, 23–26, DOI: 10.3103/S1068335620010029.
39 P. W. Bridgman, *Proc. Am. Acad. Arts Sci.*, 1925, **60**, 305–383, DOI: 10.4159/harvard.9780674287815.c27.
40 A. Coelho, *J. Appl. Crystallogr.*, 2018, **51**, 210–218, DOI: 10.1107/S1600576718000183.
41 A. Balvanz, K. S. Bayikadi, Z. Liu, T. S. Ie, J. A. Peters and M. G. Kanatzidis, *J. Am. Chem. Soc.*, 2024, **146**, 31836–31848, DOI: 10.1021/jacs.4c10872.
42 F. Maddalena, M. H. Mahyuddin, D. Kowal, M. E. Witkowski, M. Makowski, M. A. Kuddus Sheikh, S. Mahato, R. Jedrzejewski, W. Drozdowski, C. Dujardin, C. Dang and M. D. Birowosuto, *Inorg. Chem.*, 2023, **62**, 8892–8902, DOI: 10.1021/acs.inorgchem.3c00270.
43 X. Huang, B. Cheng, W. Ma, S. Qi, Y. Zhang, M. Shen, T. Bo, L. Zhang and W. Lin, *Inorg. Chem.*, 2024, **63**, 11924–11929, DOI: 10.1021/acs.inorgchem.4c01764.
44 R. Prasanna, A. Gold-Parker, T. Leijtens, B. Conings, A. Babayigit, H.-G. Boyen, M. F. Toney and M. D. McGehee, *J. Am. Chem. Soc.*, 2017, **139**, 11117–11124, DOI: 10.1021/jacs.7b04981.
45 T. Schmidt, K. Lischka and W. Zulehner, *Phys. Rev. B:Condens. Matter Mater. Phys.*, 1992, **45**, 8989–8994, DOI: 10.1103/physrevb.45.8989.
46 V. A. Fonoberov, K. A. Alim, A. A. Balandin, F. Xiu and J. Liu, *Phys. Rev. B:Condens. Matter Mater. Phys.*, 2006, **73**, 165317, DOI: 10.1103/PhysRevB.73.165317.
47 J. Li, X. Yuan, P. Jing, J. Li, M. Wei, J. Hua, J. Zhao and L. Tian, *RSC Adv.*, 2016, **6**, 78311–78316, DOI: 10.1039/c6ra17008k.
48 J. Ramade, L. M. Andriambariarijaona, V. Steinmetz, N. Goubet, L. Legrand, T. Barisien, F. Bernardot, C. Testelin, E. Lhuillier, A. Bramati and M. Chamarro, *Nanoscale*, 2018, **10**, 6393–6401, DOI: 10.1039/c7nr09334a.